Metrol. Meas. Syst., Vol. 30 (2023) No. 2, pp. 289–303
DOI: 10.24425/mms.2023.144870

PAN POLSKA AKADEMIA NAUK

METROLOGY AND MEASUREMENT SYSTEMS
Index 330930, ISSN 0860-8229
www.metrology.wat.edu.pl

M&MS

DEVELOPMENT AND PERFORMANCE TEST OF A NOVEL SOLAR TRACKING SENSOR

Jianjun Lan

Fujian Vocational & Technical College of Water Conservancy & Electric Power, School of Electric Power Engineering, Yongan 366000, China (✉ *licki518@163.com*)

Abstract

A new solar tracking sensor based on image recognition is proposed and designed to solve the problem of low accuracy of photoelectric tracking in photovoltaic power generation. The sensor can directly output its angular deviation from the sun, and its mechanical structure and working principle are analysed in detail. We use a high-precision camera to collect the image of the two slots on the projector surface and use the Hough transform to identify the image of the light seam. After obtaining the linear equation for the two slots, the coordinate of the intersection point is found, and the calculation of the solar altitude and azimuth can be realized. We have improved the Hough transform scheme by using the skeleton image of the slots instead of the edge image. The improvement of the scheme has been proved to effectively improve the detection accuracy. A calibration test board is used to test the sensor and experimental results show that the scheme can achieve the measurement of azimuth and altitude with the accuracy of be 0.05°, which can meet the detection accuracy requirements of the solar tracking in photovoltaic power generation and many other photoelectric tracking implementations.

Keywords: image recognition, photovoltaic power generation, photoelectric tracking, Hough transform.

1. Introduction

With the promotion and implementation of global energy conservation and emission reduction strategy, it is urgent to further to increase proportion of application of clean and renewable energy. *Photovoltaic* (PV) power generation as a relatively mature power generation technology will undergo rapid development. Unfortunately, due to the material and manufacturing technology of solar panels, their conversion efficiency cannot be greatly improved. However, the solar energy conversion will be maximum when the solar panel is kept perpendicular to the sun rays [1]. Therefore, many scholars focus on the research of improving the efficiency of PV systems with the application of sun tracking. Related studies show that at least 20% more electricity is produced by a tracking PV system than a fixed PV one [2, 3].

Article history: received November 29, 2022; revised January 29, 2023; accepted February 1, 2023; available online May 18, 2023.

In order to improve the efficiency of PV system, various methods of sun tracking have been used in PV systems, which includes sensorless tracking, sensor-based tracking, and hybrid tracking. The sensorless tracking method generally uses astronomic equations to determine the position of the sun [4–6], then drives the PV panels towards the sun. The sensorless tracking method does not use the additional tracking sensor, and although it has advantages in cost, the tracking accuracy is low. In order to improve tracking accuracy, more and more sensor-based tracking methods are used in sun tracking schemes and, as a result, various sun position sensors have been proposed [7].

In many studies, *light dependent resistors* (LDRs) or *photodiodes* (PDs) have been selected as light sensors for sun tracking. For instance, a one-axis three-position solar tracking system was developed in which two LDR sensors monitor the intensity of the sunlight with results that will be compared below [8]. In order to find the position of the sun precisely, an improved single-axis sun tracking system with the two identical LDRs and an angle sensor was proposed [9], including using pre-specified angles acquired by geographical positioning [10]. With the application of four LDRs, a two-axis tracking system based on Wheatstone bridge circuit without a microcontroller is proposed [11]. And on this base, the LDR arrangements and algorithm have been improved for greater detection range and higher detection accuracy, such as four quadrants and six quadrants by using the partition plate [12, 13]. At the same time, in order to reduce the effect of diffuse radiation, a sun sensor with infrared and linear polarizing optical filters was proposed [14]. In addition, because of the limitations of LDRs during overcast conditions, a novel UV sensor-based dual-axis solar tracking system was proposed which shows good potential performance [15].

No matter how the arrangements are improved, the LDRs are always distributed discretely, so the measurement accuracy cannot be greatly improved. Therefore, a method based on the *position sensitive detector* (PSD) was proposed that solved the discrete distribution problem of photoelectric devices, and the detection accuracy increased to 0.2° [16].

An omnidirectional sensor was presented in literature [17], and a photovoltaic cell was used for irradiance measurement. A quadrant sun position sensor that builds on the 3D optics approach has been reported to reach a mean error of 1.9° [18]. With the development of vision measurement technology, image measurement schemes based on cameras were used in sun tracking [19–21], so the sun's position in the sky can be determined by the captured images [22].

The literature survey indicates that as sensorless solar tracking systems are open-loop control, the tracking errors will accumulate over time, and this issue has been proved in practical application. Compared with the sensorless tracking systems, the sensor-based systems are more widely adopted. Most of the sensor-based solar tracking systems use LDRs as the tracking sensor, however, LDRs have some limitations in their application, *e.g.*, under the conditions of saturation of light intensity and low-visibility, the PV module may be directed opposite to the position of the sun [23]. Therefore, Chaowanan *et al.* [15] proposed a UV sensor-based tracking system. According to several literature reports using visual images to detect the position of the sun, when the camera faces the sun directly, the contrast of the sun images and saturation problem of the camera need to be dealt with, or else the detection accuracy cannot be significantly improved.

In this study we overcame the limitations and research deficiencies presented above by developing a novel image-based sensor that consists of a *high definition* (HD) camera and a closed container. Two vertical slots are fabricated on the top surface of the container whose function is to create a projected image of sunlight. The goal of using the projected image is to reduce the influence of background stray light and avoid the saturation of the camera. Also, the parameters of the sensor are calibrated by using the test image. The Hough transform algorithm is used to recognize the two slots in the projection image. In order to ensure the accuracy of straight-line recognition, the traditional scheme of straight line recognition after edge detection is abandoned,

Metrol. Meas. Syst., Vol. 30 (2023), No. 2, pp. 289–303
DOI: 10.24425/mms.2023.144870

and the scheme of straight line recognition after skeleton extraction is adopted. After curve fitting, the azimuth and altitude angle were measured by solving the coordinates of the intersection points of the two lines in the image. To verify the effectiveness of the sensor, evaluation tests were performed on the platform of a dual-axis solar tracking experimental system, and some concluding remarks are made at the end of this work.

2. Structure and Principle

2.1. Sensor Structure

Figure 1 shows the structure of the tracking sensor. It is made up of a camera and a sealed cylindrical container. Sunlight can enter the sensor through two vertically distributed slots and generate the projection lines on the bottom surface. The camera is embedded in the centre of the container's top surface to capture the image of the light projection on the bottom surface.

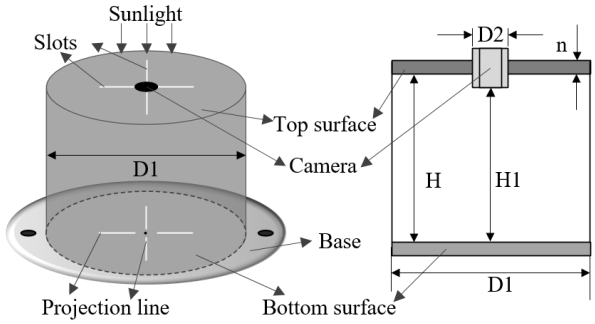

Fig. 1. Structure of proposed tracking sensor.

2.2. Working principle

Figure 2 shows the angle calculation schematic diagram. O_1 is defined at the centre of the top surface, $O_2(0, 0)$ is defined at the centre of the bottom surface. When the sun shines vertically, the

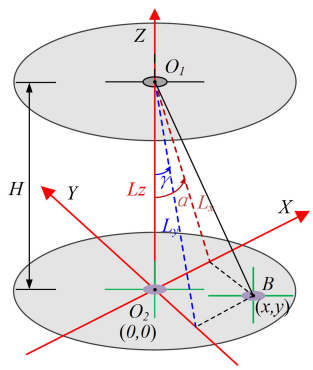

Fig. 2. Angle calculation schematic diagram.

intersection point of the projected lines is at the centre (point O_2) of the bottom surface. While the sun shines obliquely, the intersection point will deviate from the centre of the bottom surface. Suppose the intersection moves to point $B(x, y)$, the azimuth and altitude can be calculated as follows:

$$\begin{cases} \alpha = \arctan(x/z) \\ \gamma = \arctan(y/z) \end{cases}, \tag{1}$$

where, α is azimuth, and γ is altitude.

2.3. Coordinate Measurement

Figure 3 shows the schematic diagram of the pinhole model. $O_w - X_w Y_w Z_w$ is the world coordinate system, $O_c - X_c Y_c Z_c$ is the camera coordinate system, $O_p - X_p Y_p Z_p$ is the image coordinate system, and O-UV is the pixel coordinate system. O_c is the camera optical center, and $O_c Z_c$ is the camera's optical axis. Assuming that point p is a point in the world coordinate system, and its coordinates in the camera coordinate system and the world coordinate system are (X_c, Y_c, Z_c) and (X_w, Y_w, Z_w) respectively, similarly, the coordinates of the image point p' in image coordinate system and pixel coordinate are (x, y) and (u, v).

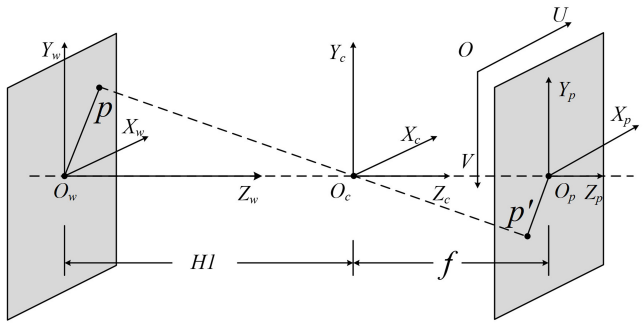

Fig. 3. Schematic diagram of the pinhole imaging model.

According to the cubic coordinate transformation relationship [13], the conversion relationship between the world coordinates and the camera coordinates can be described by (2).

$$\begin{bmatrix} X_c \\ Y_c \\ Z_c \end{bmatrix} = R \begin{bmatrix} X_w \\ Y_w \\ Z_w \end{bmatrix} + T, \tag{2}$$

where R is the rotation matrix, and T is the translation matrix.

The conversion relationship between the camera coordinate and the image coordinate is shown in (3).

$$Z_c \begin{bmatrix} x \\ y \\ 1 \end{bmatrix} = \begin{bmatrix} f/dx & 0 & u_0 & 0 \\ 0 & f/dy & v_0 & 0 \\ 0 & 0 & 1 & 0 \end{bmatrix} \begin{bmatrix} X_c \\ Y_c \\ Z_c \\ 1 \end{bmatrix}, \tag{3}$$

where f is the focal length of the camera, dx and dy are pixel sizes in pick x and y, while u_0 and v_0 are coordinates in the pixel coordinate.

Metrol. Meas. Syst., Vol. 30 (2023), No. 2, pp. 289–303
DOI: 10.24425/mms.2023.144870

The image coordinate and the pixel coordinate are in the same plane, only units and origin are different. So, their relationship can be expressed by (4).

$$\begin{bmatrix} u \\ v \\ 1 \end{bmatrix} = \begin{bmatrix} \frac{1}{dx} & 0 & u_0 \\ 0 & \frac{1}{dy} & v_0 \\ 0 & 0 & 1 \end{bmatrix} \begin{bmatrix} x \\ y \\ 1 \end{bmatrix}. \tag{4}$$

3. Sensor Assembling and Calibration

3.1. Mechanical dimension setting

The main task is the assembly of mechanical components of sensors. The most important parts are the fixation of the camera and the adjustment of the size parameters. The HD camera used in this project is an OV5640 mini camera and the key typical specifications are shown in Table 1.

Table 1. The key typical specifications of OV5640.

Type	Value	Type	Value
Active array size	2592 × 1944	Image area	3673.6 μm × 2738.4 μm
Lens size	1/4 Inch	Pixel size	1.4 μm × 1.4 μm

The goal of sensor's dimensions debugging is to improve the detection accuracy while ensuring the maximum field of view of the camera. According to the experimental test data, the final size parameters of the sensor are shown in Table 2.

Table 2. Size parameters of the sensor.

Type	Value	Type	Value
Top surface height (H)	89.0 mm	Bottom surface diameter (D1)	100.0 mm
Camera height (H1)	80.0 mm	Slot length (L)	15.0 mm
Top surface diameter (D1)	100.0 mm	Slot width (d)	1.0 mm

3.2. Parameter Calibration

In order to solve the azimuth and altitude angle, (1)–(4) are required to convert the coordinates in the pixel coordinate system to the world coordinate system simultaneously, so the parameters in the equation above need to be calibrated and solved. It is required to solve the (1)–(4) to convert the pixel coordinate to the world coordinate, so the parameters in the above equations need to be determined by the way of calibration. Since the top surface, bottom surface and the camera mirror are parallel and fixed in distance, the matrix R and T can be ignored, and the focal length is the only unknown parameter.

The focal length of the camera can be calculated with (5), according to the camera's active array size, pixel size and the information of the test image shown in Fig. 4, $f = 1944 \times 1.4\ \mu\text{m} \times 80.00\ \text{mm}/100.0\ \text{mm} = 2.18\ \text{mm}$.

$$f = \frac{P \times D}{W}, \tag{5}$$

where P is the length of image, D is the object distance, W is the actual object width.

Meanwhile, according to the image information shown in Fig. 4, the centre point (1263, 934) of the calibration image captured by the camera is not the pixel centre point (1296, 972) of the camera. The reason is that when the camera is fixed, it cannot be in the mechanical centre of the sensor. Therefore, the angle calculation needs to be corrected according to the deviation.

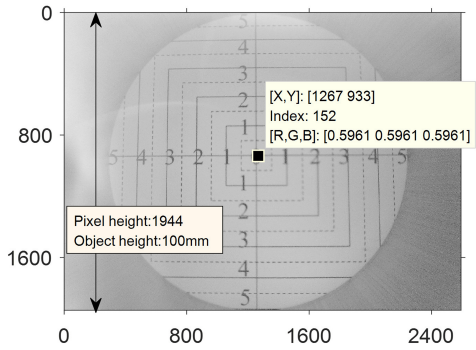

Fig. 4. Test image of the sensor.

4. Angle Measurement

4.1. Line recognition

The Hough transform is one of the most commonly used methods for line detection in images, the basic principle is to extract the straight-line edge in the binary image and then use the "houghlines" function in MATLAB to find the endpoints of the line segments corresponding to peaks in the Hough transform [24, 25]. Fig. 5a shows the original image of the slot projection. As the sensor structure is closed, the camera is less affected by the ambient light and the background segmentation is simple. The edge extraction can be performed only after the necessary image pre-processing such as grey transformation, binarization and morphological filtering. Figs. 5b–5d respectively show the effect images after pre-processing.

In the process of edge extraction, the "Canny" operator is used to obtain the contours and the gradient map of the line area respectively, and the edge contour of this area can be obtained [26]. The Hough transform is employed to identify line segments, from which the slot projection can be reconstructed [27]. Since the endpoints of the identified line segments are located on the edge of the image contour, it is natural that the identified lines are not the centre lines of the slot projection, and this causes a great error in the coordinate values calculation of the intersection point of the projection lines.

Figure 6 shows the effect diagram of traditional Hough transform line recognition. According to the effect diagram, the line fitted by Hough transformation is located at the edge of the image, and there is a large error in the calculation of the intersection coordinates.

Metrol. Meas. Syst., Vol. 30 (2023), No. 2, pp. 289–303
DOI: 10.24425/mms.2023.144870

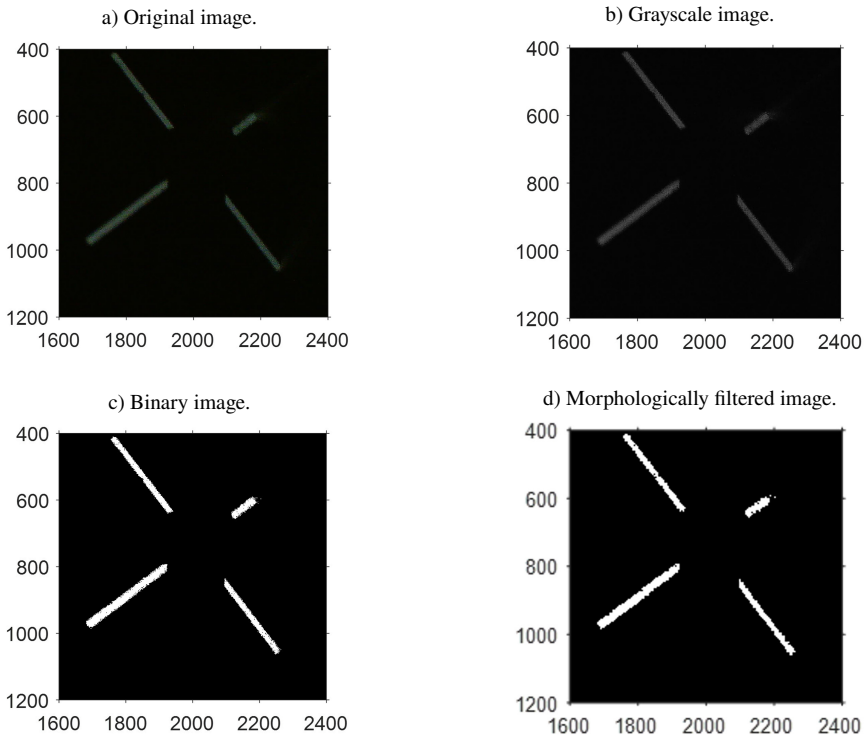

Fig. 5. Comparison of the original image and the pre-processed images.

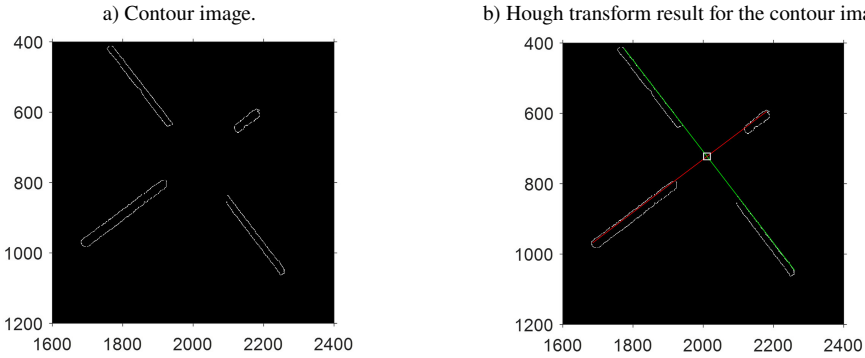

Fig. 6. Resulting diagrams of traditional Hough transform line recognition.

Therefore, we propose a method to detect straight lines by using the skeleton image instead of the edge image in the Hough transform. The skeleton of the image is the central axis of the image, so the central axis of the slot image can be obtained after skeleton extraction. We use the "bwmorph()" function provided in the MATLAB image toolbox for the mathematical deformation of the projected image, and select the parameter "thin" as the operation type, the parameter "inf" as the number of operations. This method can ensure that the identified line segment is located

on the centre line of the slot projection image and greatly reduces the detection time, the effect diagram of the improved Hough transform is shown in Fig. 7.

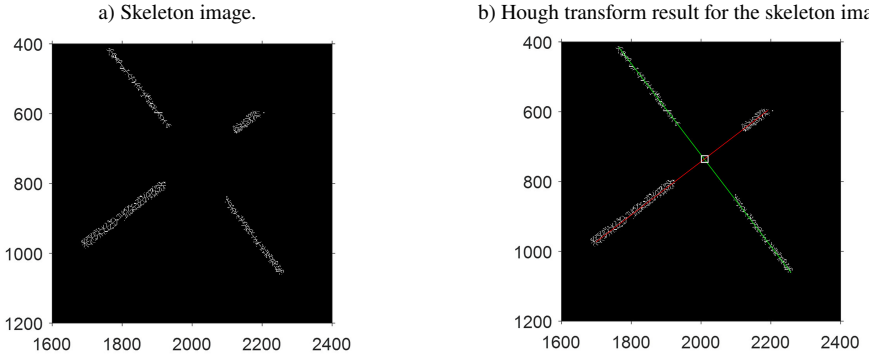

Fig. 7. Resulting diagrams of the improved Hough transform.

4.2. Angle Calculation

The coordinates of the intersection point of the central axes of the lines identified in Fig. 8 can be substituted into (2)–(4) successively after deviation correction. Next, the coordinate values in the world coordinate system of the centre point of the projection can be calculated, and the azimuth and altitude can be solved with (1).

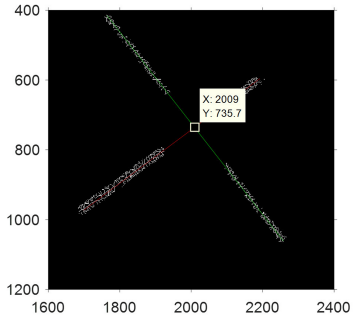

Fig. 8. Identification results of centre line intersection.

5. Experiment and Analysis

5.1. Experiment Settings

We validated the presented sensor on the two-axle sun tracking experimental platform. An OV5640 mini HD camera was selected as the acquisition device of the projection images An MPU9250 nine-axis inertial sensor mounted on the sensor surface was used to measure the yaw and roll of the solar panel, and its outputs were used for the error evaluation of the sun tracking sensor. The control core of the system was JETSON NANO, to which the servos of the experimental, MPU9250 and the proposed sensor were all connected. All the used experimental devices are shown in Fig. 9.

Metrol. Meas. Syst., Vol. 30 (2023), No. 2, pp. 289–303
DOI: 10.24425/mms.2023.144870

a) Two-axle sun tracking experimental facility.

b) Proposed sensor.

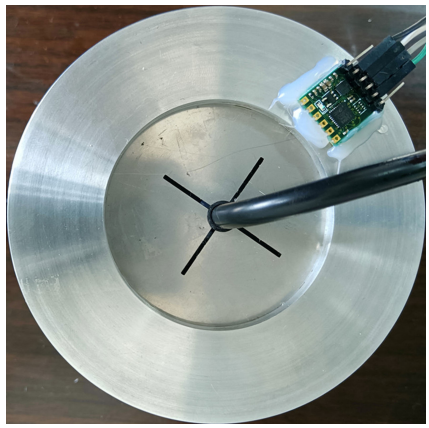

c) JETSON NANO 4GB.

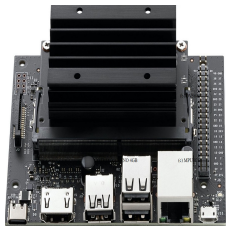

d) OV5640.

e) MPU 9250.

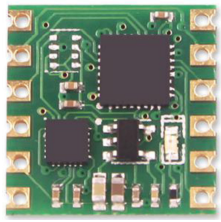

f) A 9W LED.

Fig. 9. Experimental devices used.

5.2. Experimental testing and analysis

Since the angle of the sunlight changes at all times, it was not suitable for sensor calibration, so the LED source was selected to simulate the sunlight in the experimental test. The LED source was set directly above the proposed sensor, and the experimental device was rotated in the east-west and north-south directions at a step angle of 5° each time, and the measured values of the MPU9250 and the sensor proposed in this paper were recorded respectively. The test diagram of rotation operation is shown in Fig. 10, and the error curves are shown in Fig. 11.

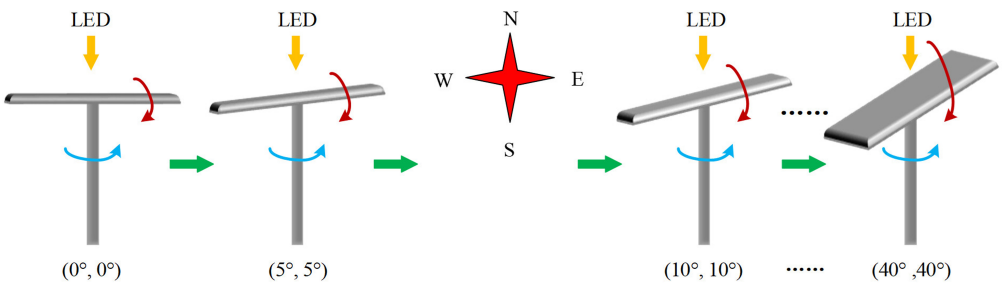

Fig. 10. Schematic diagram of the rotary operation test.

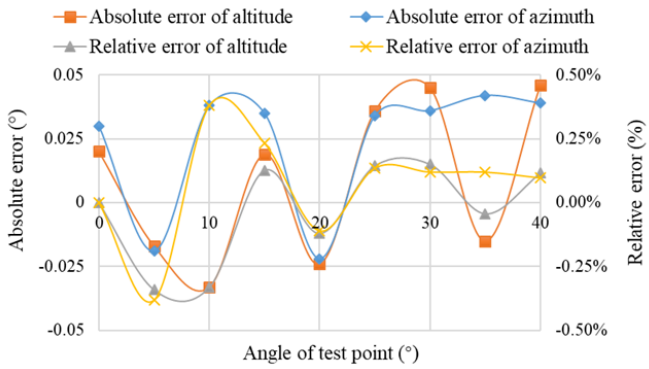

Fig. 11. Error curves.

When analysing the angle calculation formula shown in (1), we learn that the angle measurement error mainly comes from the camera installation height error and image centre coordinate positioning error. Although the error of the centre position during camera installation may also cause error, it can be eliminated by the way of zero adjustment. Therefore, it is necessary to focus on the influence of camera height error and image centre coordinate positioning error on sensor measurement error.

5.2.1. Analysis of the influence of camera mounting height on error

Figure 12 shows the angle measurement error relation curve generated by the deviation of different image centre position and camera installation height. The image centre is in different positions, although the camera installation height deviation is the same, but the impact on the angle measurement error is different. As the error distribution curves of high and low installation height are symmetrical, only the angle measurement error curve between the high camera position and the centre position of the sensor is given. When the camera installation height error is less than 0.2 mm, the angle measurement error is no more than 0.05 degrees. When the camera height deviation is greater than 0.5 mm, the angle measurement error increases significantly. Therefore,

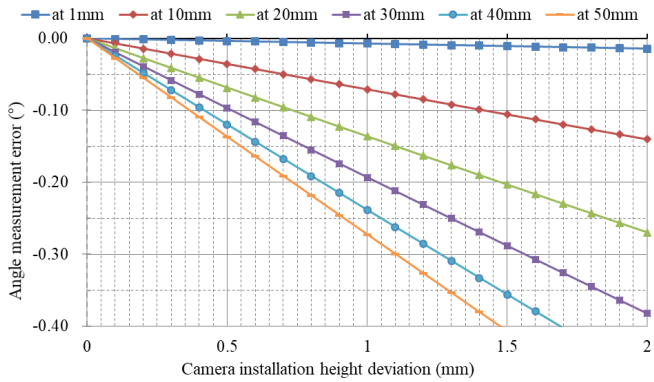

Fig. 12. Error curve of different image center position and camera installation height deviation.

Metrol. Meas. Syst., Vol. 30 (2023), No. 2, pp. 289–303
DOI: 10.24425/mms.2023.144870

in order to improve the measurement accuracy, the measurement range of the sensor should be within 15 degrees as far as possible.

5.2.2. Analysis of the influence of image centre coordinate location on error

Figure 13 shows the positioning error curve of image centre position and centre coordinate. According to the curve in the figure, when the accuracy of image recognition pixel remains within 1 pixel, the error of angle measurement will not be greater than 0.05 degrees.

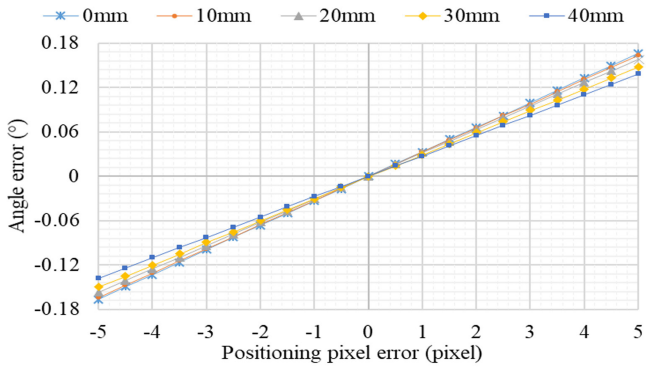

Fig. 13. Error curve of image centre position and centre coordinate positioning.

5.3. Application test

In order to investigate the working effect of the practical application of the sensor, we tested the practical application of the sensor respectively under four lighting conditions: sunny, cloudy, local shadow and overcast day. The application test resulting diagram is shown in Fig. 14. We give the original image, binarization image and line recognition result image under each weather condition. Because the light is too weak in cloudy days, the straight line cannot be identified by morphological filtering with the fixed threshold value. Therefore, a dynamic average value scheme is adopted in threshold setting.

a) Test results on sunny days.

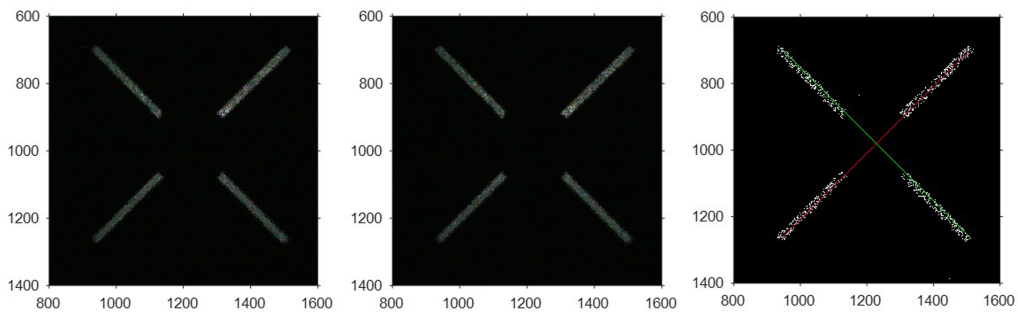

b) Test results on cloudy days.

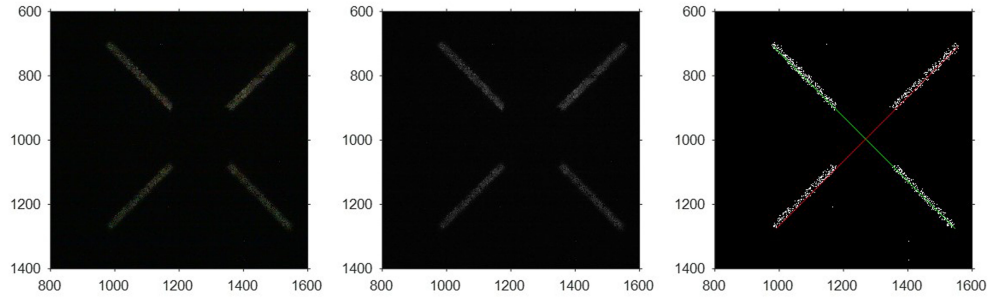

c) Test results for local shadow.

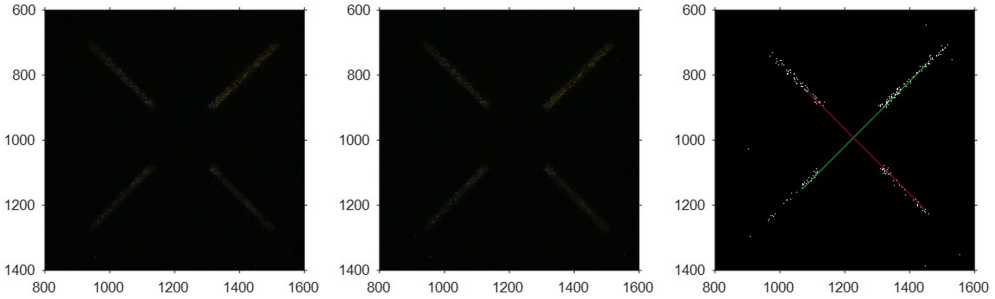

d) Test results on overcast days.

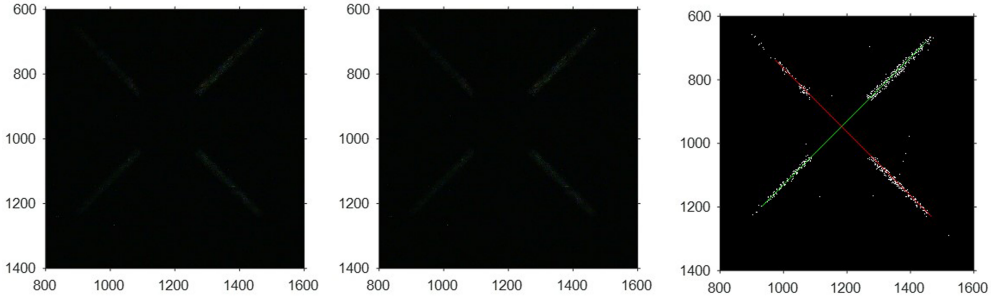

Fig. 14. Application test result diagram (from left to right: original image, binarization image and line recognition result).

6. Conclusions

A novel solar tracking sensor was successfully developed and applied using the unique shape structure and a high precision camera, which eliminated the need for complex logical evaluation of the sun's direction. The sensor structure is simple, and the sensor has the advantages of high accuracy of solar tracking (maximum error of position detection is 0.05°) and relatively simplicity in image processing. The detection accuracy of the sensor is greatly affected by the deviation range of the sun's direction, so the sensor can only achieve high precision detection when the deviation range is small. However, we believe that in practical applications, the photovoltaic tracking controller can easily adjust the deviation range to a small range through 1–2 tracking control periods. Therefore, the practical application of the sensor will not be limited.

Metrol. Meas. Syst., Vol. 30 (2023), No. 2, pp. 289–303
DOI: 10.24425/mms.2023.144870

References

[1] Walczak, M., Bychto, L., & Kraniewski, J. (2022). Design and Evaluation of a Low-Cost Solar Simulator and Measurement System for Low-Power Photovoltaic Panels. *Metrology and Measurement Systems*, *29*(4), 685–700. https://doi.org/10.24425/mms.2022.143067

[2] Mah, A. X. Y., Ho, W. S., Hassim, M. H., & Hashim, H. (2021). Optimization of Photovoltaic Array Orientation and Performance Evaluation of Solar Tracking Systems. *Chemical Engineering Transactions*, *83*, 109–114. https://doi.org/10.3303/CET2183019

[3] Gutierrez, S., Rodrigo, P. M., Alvarez, J., Acero, A., & Montoya, A. (2020). Development and testing of a single-axis photovoltaic sun tracker through the Internet of Things. *Energies*, *13*(10), 2547. https://doi.org/10.3390/en13102547

[4] Zhao, D., Xu, E., Wang, Z., Yu, Q., Xu, L., & Zhu, L. (2016). Influences of installation and tracking errors on the optical performance of a solar parabolic trough collector. *Renew Energy*, *94*, 197–212. https://doi.org/10.1016/j.renene.2016.03.036

[5] Melo, K., Tavares, L. R., & Villalva, M. G. (2021). Statistical Analysis of Solar Position Calculation Algorithms: SPA and Grena 1-5. *IEEE Latin America Transactions*, *19*(7), 1145–1152. https://doi.org/10.1109/TLA.2021.9461843

[6] Miotto, M., Gonzatti, F., Franchi, D., da Silva, E. I., & Farret, F. A. (2021). Pseudo-azimuthal dual-axis solar tracking technique using the hourly method for photovoltaic modules. *Journal of Control, Automation and Electrical Systems*, *32*, 983–991. https://doi.org/10.1007/s40313-021-00721-0

[7] Salgado-Conrado, L. (2018). A review on sun position sensors used in solar applications. *Renewable and Sustainable Energy Reviews*, *82*, 2128–2146. https://doi.org/10.1016/j.rser.2017.08.040

[8] Parthipan, J., Raju, B. N., & Senthilkumar, S. (2016). Design of one axis three position solar tracking system for paraboloidal dish solar collector. *Materials Today: Proceedings*, *3*(6), 2493–2500. https://doi.org/10.1016/j.matpr.2016.04.167

[9] Kabalci, E., & Calpbinici, A. (2020). Design and Implementation of Control Algorithms for Single-Axis Sun Tracking Systems. *Journal of Power Technologies*, *100*(1), 32–42. https://papers.itc.pw.edu.pl/index.php/JPT/article/view/1460

[10] Jamroen, C., Komkum, P., Kohsri, S., Himananto, W., Panupintu, S., & Unkat, S. (2020). A low-cost dual-axis solar tracking system based on digital logic design: Design and implementation. *Sustainable Energy Technologies and Assessments*, *37*, 100618. https://doi.org/10.1016/j.seta.2019.100618

[11] Saeedi, M., & Effatnejad, R. (2021). A new design of dual-axis solar tracking system with LDR sensors by using the wheatstone bridge circuit. *IEEE Sensors Journal*, *21*(13), 14915–14922. https://doi.org/10.1109/JSEN.2021.3072876

[12] Canada-Bago, J., Fernandez-Prieto, J. A., Gadeo-Martos, M. A., & Perez-Higueras, P. (2020). Knowledge-Based Sensors for Controlling A High-Concentration Photovoltaic Tracker. *Sensors*, *20*(5), 1315. https://doi.org/10.3390/s20051315

[13] Dadi, V., & Peravali, S. (2020). Optimization of light-dependent resistor sensor for the application of solar energy tracking system. *SN Applied Sciences*, *2*(9), 1499. https://doi.org/10.1007/s42452-020-03293-x

[14] Diaz, A., Garrido, R., & Soto-Bernal, J. J. (2018). A filtered sun sensor for solar tracking in HCPV and CSP systems. *IEEE Sensors Journal*, *19*(3), 917–925. https://doi.org/10.1109/JSEN.2018.2879460

[15] Jamroen, C., Fongkerd, C., Krongpha, W., Komkum, P., Pirayawaraporn, A., & Chindakham, N. (2021). A novel UV sensor-based dual-axis solar tracking system: Implementation and performance analysis. *Applied Energy*, *299*, 117295. https://doi.org/10.1016/j.apenergy.2021.117295

[16] Wang, Y., Yu, X., Wang, D., Feng, Q., & Shi, Y. (2019). Analog Detection of PSD Sensor and Sunshine Position Tracking Performance in Four Quadrant Arrays. *International Journal of Performability Engineering*, *15*(9), 2346. https://doi.org/10.23940/ijpe.19.09.p7.23462355

[17] Gómez-Uceda, F. J., Ramirez-Faz, J., Varo-Martinez, M., & Fernández-Ahumada, L. M. (2021). New omnidirectional sensor based on open-source software and hardware for tracking and backtracking of dual-axis solar trackers in photovoltaic plants. *Sensors*, *21*(3), 726. https://doi.org/10.3390/s21030726

[18] Romijn, J., Vollebregt, S., May, A., Erlbacher, T., van Zeijl, H. W., Leijtens, J., ... & Sarro, P. M. (2022, January). Visible Blind Quadrant Sun Position Sensor in a Silicon Carbide Technology. In *2022 IEEE 35th International Conference on Micro Electro Mechanical Systems Conference* (MEMS) (pp. 535–538). IEEE. https://doi.org/10.1109/MEMS51670.2022.9699533

[19] Hamouda, A., Ababneh, M., Zahrani, M. A., & Chabchoub, A. (2020). Fuzzy Controller for Sun Tracking (Using Image Processing). In *Intelligent Systems and Applications: Proceedings of the 2019 Intelligent Systems Conference (IntelliSys) Volume 2* (pp. 1258–1266). Springer International Publishing. https://doi.org/10.1007/978-3-030-29513-4_92

[20] Ruelas, A., Velázquez, N., Villa-Angulo, C., Acuña, A., Rosales, P., & Suastegui, J. (2017). A solar position sensor based on image vision. *Sensors*, *17*(8), 1742. https://doi.org/10.3390/s17081742

[21] Angulo, M., Díaz-Ponce, A., Valentín, L., Valdivia, R., & Keshtkar, S. (2020). Design and Control of a Passive Solar Tracking System Using a Sky Imager. In *Industrial and Robotic Systems: LASIRS 2019* (pp. 170–178). Springer International Publishing. https://doi.org/10.1007/978-3-030-45402-9_17

[22] Carballo, J. A., Bonilla, J., Roca, L., & Berenguel, M. (2018). New low-cost solar tracking system based on open source hardware for educational purposes. *Solar Energy*, *174*, 826–836. https://doi.org/10.1016/j.solener.2018.09.064

[23] Kuttybay, N., Saymbetov, A., Mekhilef, S., Nurgaliyev, M., Tukymbekov, D., Dosymbetova, G., ... & Svanbayev, Y. (2020). Optimized single-axis schedule solar tracker in different weather conditions. *Energies*, *13*(19), 5226. https://doi.org/10.3390/en13195226

[24] Li, X., Su, J., Yue, Z., Wang, S., & Zhou, H. (2022). Extracting navigation line to detect the maize seedling line using median-point Hough transform. *Nongye Gongcheng Xuebao/Transactions of the Chinese Society of Agricultural Engineering*, *38*(5), 167–174. https://doi.org/10.1590/0103-8478cr20190699

[25] Zhuo, H. B., Bai, F. Z., & Xu, Y. X. (2020). Machine vision detection of pointer features in images of analog meter displays. *Metrology and Measurement Systems*, *27*(4), 589–599. https://doi.org/10.24425/mms.2020.134840

[26] Quan, P., Lin, H., Liang, Z., & Di, S. (2021). Research on fast identification and location of contour features of electric vehicle charging port in complex scenes. *IEEE Access*, *10*, 26702–26714. https://doi.org/10.1109/ACCESS.2021.3092210

[27] Reiter, T., McCann, M., Connolly, J., & Haughey, S. (2021). An Investigation of Edge Bead Removal Width Variability, Effects and Process Control in Photolithographic Manufacturing. *IEEE Transactions on Semiconductor Manufacturing*, *35*(1), 60–66. https://doi.org/10.1109/TSM.2021.3129770

Metrol. Meas. Syst., Vol. 30 (2023), No. 2, pp. 289–303
DOI: 10.24425/mms.2023.144870

Jianjun Lan obtained the B.Eng. and M.Eng. degrees in control engineering from the Northeast Electric Power University (NEEPU), China, in 2002 and 2009, respectively. He is currently Assistant Professor with the Fujian College of Water Conservancy and Electric Power, China. His research activity focuses on photoelectric detection, and control of new energy generation technology.